SCIENCE CHINA
Information Sciences

· Supplementray File ·

Dynamic switching and oxygen ion transport in $(Hf+Zr)O_{2-x}$ ferroelectrics modulated by Al_2O_{3-x} interfaces

Ze FENG[1,4], Huan LIU[2], Weiwen PAN[2], Boyuan ZHANG[1], Ao LIU[1], Xu ZHENG[1], Yiyang SHAN[1], Xiang ZHAO[1], Rong HUANG[3], Weihua WWANG[1], Yahui CHENG[1], Feng LU[1], Yi CUI[3], An DINGSUN[5], Genquan HAN[2,*], Hui LIU[,*] and Hong DONG[1,*]

1. Engineering Research Center of Thin Film Optoelectronics Technology, Ministry of Education, Nankai University, Tianjin, 300350, China
2. Hangzhou Institute of Technology, Xidian University, Hangzhou 311231, China
3. Suzhou Institute of Nano-Tech and Nano-Bionics (SINANO), Chinese Academy of Sciences, Suzhou 215123, China
4. Institute of Intelligent Photonics, Nankai University, Tianjin, 300071, China
5. School of Integrated Circuits, Nanjing University, Suzhou 215163, China

Appendix A Device Fabrication Process

Prior to film deposition, an 8-inch Si wafer was ultrasonically cleaned by acetone, methanol, and isopropyl alcohol for 1 min each at room temperature and blown dry with high-purity nitrogen gas (99.9999%). A 70 nm TiN (bottom electrode) layer was deposited at room temperature via direct current sputtering (Figure S14). The 8 nm thick $(Hf+Zr)O_{2-x}$ thin film was then deposited on bottom electrode. The atomic layer deposition (ALD) process was carried out with TDMA-Zr (300 ms pulse)/N_2 purge (8 s)/$H_2{}^{16}O$ (30 ms pulse)/N_2 purge (8 s)/TDMA-Hf (100 ms pulse)/N_2 purge (8 s)/ $H_2{}^{16}O$ (30 ms pulse)/N_2 purge (8 s) squence for 80 cycles. The growth rate of ALD of $(Hf+Zr)O_{2-x}$ was calibrated to be 0.1 nm/cycle. 3 cycles of ALD of alumina CL was then grown on the samples with the temperature maintained at 250 °C. The ALD recipe consisted of a 50 ms TMA pulse/12 s N_2 purge/50 ms (or 10 ms) H_2O pulse/12 s N_2 purge. High purity N_2 gas was served as the carrier and purge gas with a gas flow of 50 SCCM. Then all samples were divided into two groups. One group undergoes the rapid thermal annealing (RTA, LRTP1200, Joule Yach) at 550 °C for 30 s in N_2 atmosphere before the W top electrode (TE) deposition. The other group was annealed at the same condition after TE deposition. W electrode was deposited via direct current sputtering (FJL560C) using a shadow mask with the diameter of 200 um (base pressure during the sputtering process ~10^{-3} Torr).

The crystalline structure was characterized by GIXRD using the SmartLab diffractometer with Cu $K\alpha_1$ radiation (λ = 1.5406 Å) at 9 kW power, employing a grazing incidence angle of 0.5°. XPS measurements were carried out using PHI 5000 Versa Probe III equipped with a monochromatic Al $K\alpha_1$ radiation source of 1486.7 eV. The hemispherical analyzer was operating at constant analysis energy mode. The pass energy of all high resolution XPS spectra was 23.50 eV and the step size was set to be 0.1 eV. In order to characterize the elemental depth profile, the take off angle (sample surface to the electron analyzer) were taken at 45° and 90°. AAnalyzer was used as the

peak-fitting software for the deconvolution of the XPS and GIXRD spectra. Depth profiling measurements were performed using TOF.SIMS 5-100 instrument equipped with a 15 keV Bi^+ primary beam and a 1 keV Cs^+ sputtering beam. The system achieved a detection limit at the ppm to ppb level, depth resolution better than 1 nm, and a minimum beam diameter of less than 90 nm. The *P-V* measurements were performed using dynamic hysteresis measurement modules with a TF Analyzer 3000 in the ambient atmosphere at room temperature. The back electrode of TiN was grounded and the direct current bias voltage was applied on the W top electrode for all measurements. The *I−V* characterization was conducted using a low-noise Keithley 4200 semiconductor parameter analyzer.

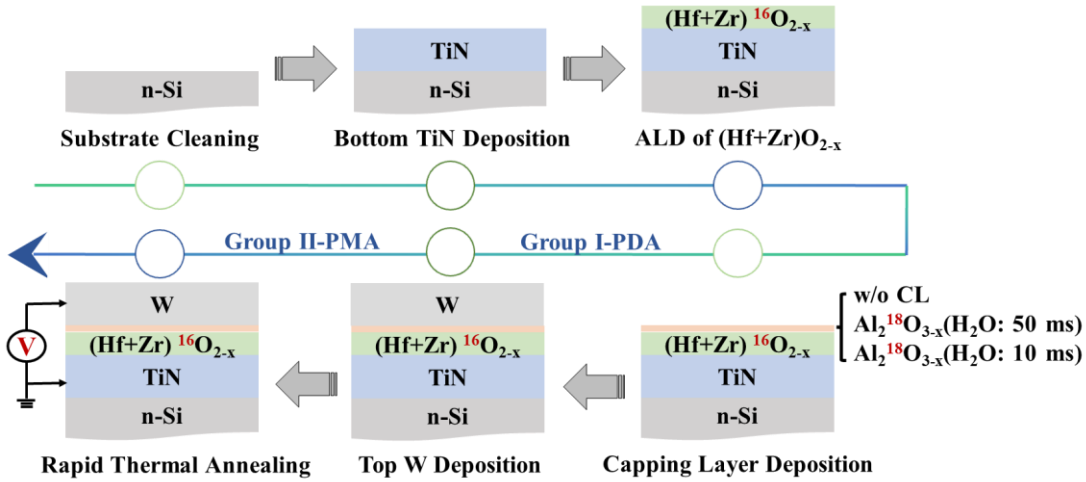

Figure A1 Flow chart of the fabrication process of the W/CL/(Hf+Zr)O_{2-x}/TiN capacitor (CL: w/o CL, 3 cycles of Al_2O_{3-x} (H_2O: 50 ms), and 3 cycles of Al_2O_{3-x} (H_2O: 10 ms)).

Appendix B Basic Electrical Characteristics

Figure B1 presents the *P-V* curves of W/CL/(Hf+Zr)O_{2-x}/TiN capacitors at various scanning voltages after the PMA/PDA treatment, with a test frequency of 1 kHz. The corresponding *I-V* curve can be found in figure B2. For the PMA-treated samples, the P_r of the reference sample is approximately 20.6 μC/cm^2 under 3 MV/cm scanning voltage. The insertion of 3 cycles of atomic layer deposition (ALD) of Al_2O_{3-x} (H_2O: 50 ms) layer increases the P_r of the device by ~3.9% and the E_c by ~2%. In contrast, the insertion of 3 cycles of ALD of Al_2O_{3-x} (H_2O: 10 ms) layer results in an ~8.7% increase in P_r and a reduction in E_c by ~1.4%. For the PDA-treated samples, the P_r of the reference sample is ~7.3 μC/cm^2 under 3 MV/cm scanning voltage. Here, the insertion of the CL slightly increases the P_r but significantly increases the E_c. Specifically, the sample with 3 cycles of Al_2O_{3-x} (H_2O: 50 ms) CL exhibits a P_r of 13.2 μC/cm^2, while the sample with 3 cycles of Al_2O_{3-x} (H_2O: 10 ms) CL shows a P_r value of 11.7μC/cm^2.

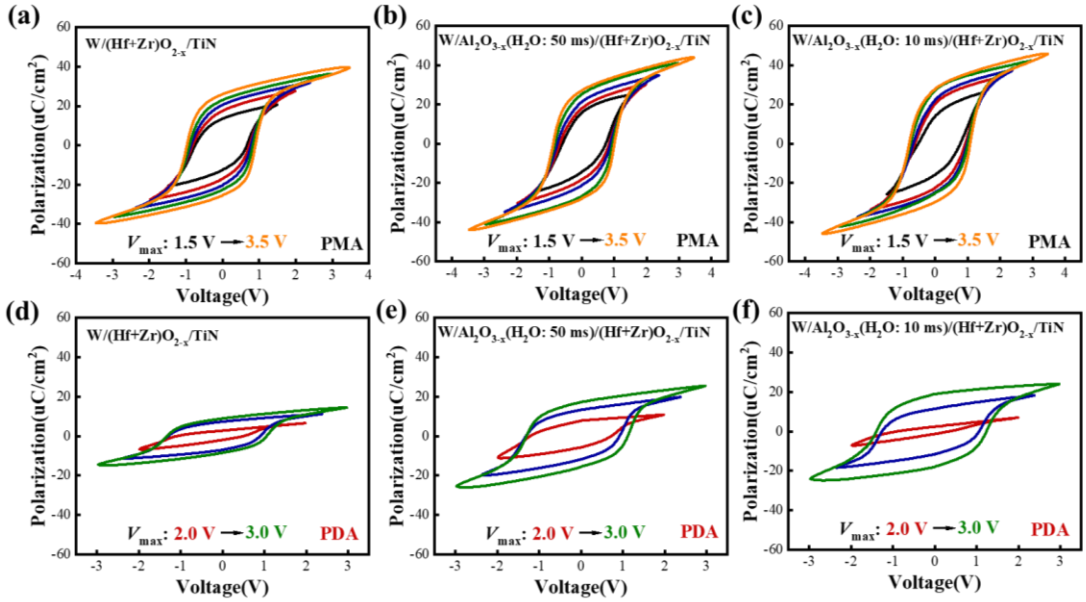

Figure B1 Measured *P-V* curves of W/CL/(Hf+Zr)O_{2-x}/TiN capacitor after the (a)-(c) PMA and (d)-(f) PDA treatment.

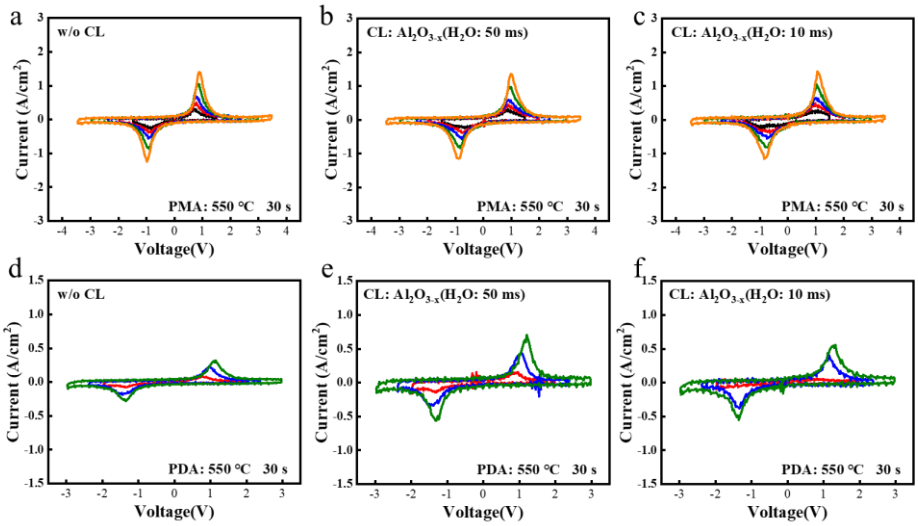

Figure B2 Measured *I-V* curves of W/CL/(Hf+Zr)O_{2-x}/TiN capacitor (CL: w/o CL, Al_2O_{3-x} (H_2O: 50 ms), and Al_2O_{3-x} (H_2O: 10 ms)) after the (a-c) PMA and (d-f) PDA treatment.

It has been reported that density of interfacial defects are highly sensitive to variations in frequency [1, 2]. Figure B3(a) depicts the *P-V* hysteresis curves of capacitors at varying frequencies after the PMA/PDA treatment, with measurement frequencies ranging from 500 Hz to 100 kHz. As the frequency increases, the pulse width gradually decreases, resulting in changes in the measured switchable polarization ($2P_r$ value) and a significant broadening of *P-V* hysteresis loops. The $2P_r$ value increases slightly with the test frequency increases for the reference sample. In contrast, the $2P_r$ value of capacitors with CL is notably higher at a frequency of 500 Hz compared to that observed at higher frequencies. This frequency response of the $2P_r$ value differs markedly from the reference sample and the previously reported $Hf_{0.5}Zr_{0.5}O_2$ results in the literature, suggesting that additional polarization mechanisms beyond ferroelectric dipoles may contribute to the observed behavior in this stack [3, 4]. For the PDA-treated samples,

the $2P_r$ value of the sample with CL shows slightly decrease with frequency increases. Similar with the corresponding PMA-treatment sample, the sample with Al_2O_{3-x} CL exhibits a pronounced decrease in the $2P_r$ value as frequency increases. This behavior originates from the oxygen-deficient state of the Al_2O_{3-x} CL and its interfacial chemistry with both the $(Hf+Zr)O_{2-x}$ layer and electrodes.

The variation of the E_c value of the devices with respect to the frequency is shown in Figure B3(b). For the PMA-treated samples, as the test frequency increases from 500 Hz to 100 kHz, the E_c^+ (E_c^-) for the reference sample exhibits increments of 75% (85%). In contrast, the devices with the Al_2O_{3-x} (H_2O: 50 ms) layer show increments of 68% (76%), which are slightly greater than the corresponding increments of 55% (69%) observed in devices with an Al_2O_{3-x} (H_2O: 10 ms) layer. For the PDA-treated samples, the increment of E_c^+ (E_c^-) for the capacitor with the Al_2O_{3-x} (H_2O: 50 ms) layer is 22% (27%) as the test frequency increases from 500 Hz to 100 kHz, slightly higher than the corresponding 8% (13%) increment for the capacitor with the Al_2O_{3-x} (H_2O: 10 ms) layer. Both sets of capacitor devices exhibit two distinct scaling regions in *P-V* curves, and significant differences in the broadening of the *P-V* curves can be observed among the various samples. This suggests that the internal defects at the CL/$(Hf+Zr)O_{2-x}$ interface are responsible for the observed difference, rather than external defects induced by frequency variations [3, 5]. The broadening of the *P-V* curves and the significant increase in E_c values at higher test frequencies are closely related to the gradual attenuation of defect dynamic behavior [3, 6, 7]. For PMA-treated samples, it is evident that the capacitor with Al_2O_{3-x} (H_2O: 10 ms) CL have lower E_c at the same frequency compared to the sample with Al_2O_{3-x} (H_2O: 50 ms) CL. Besides, compared to PMA-treat samples, the insertion of the CL results in a higher E_c at low frequencies for the PDA-treated samples, which may be associated with difference in proportion of crystalline in $(Hf+Zr)O_{2-x}$ films after the PDA treatment. Typically, both charge trapping/detrapping and ion/vacancy migration behaviors in the stack can lead to alterations in the $2P_r$ and E_c values [3, 8, 9]. Based on this, performing detailed interfacial chemical analysis of the stack after CL deposition and annealing process, as well as element distribution mapping under varying polarization states, is essential for further understanding the frequency-dependent *P-V* test results.

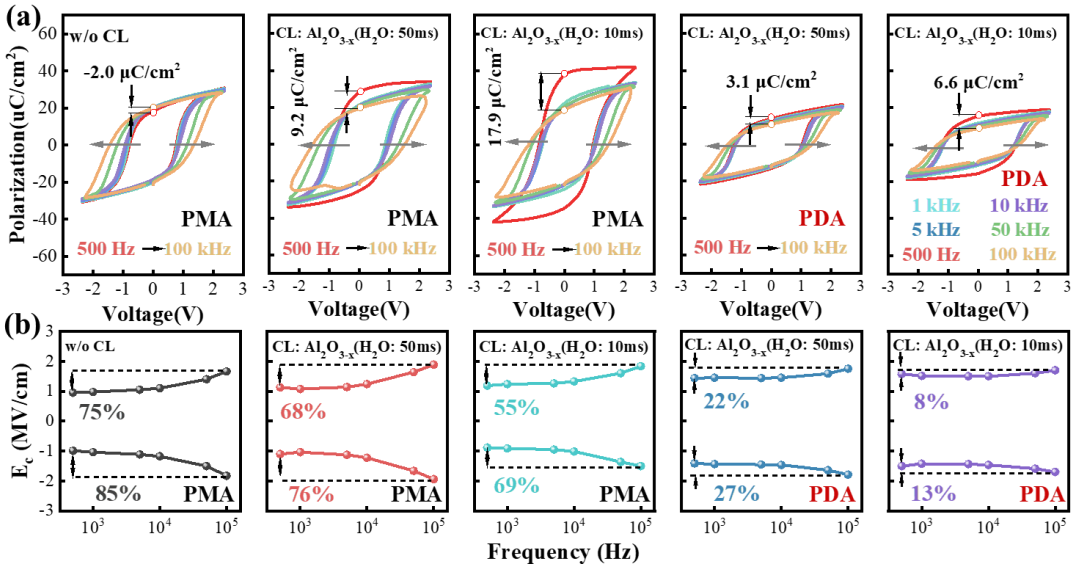

Figure B3 (a) Measured the *P-V* curves of CL/(Hf+Zr)O_{2-x} capacitors after the PMA and PDA treatment at the different frequencies. (b) Extracted the E_c versus frequency of the devices.

As shown in Figure B4, the PDA-treated samples with CL insertion exhibit superior endurance performance relative to PMA-treated samples, in agreement with established literature reports [10]. During the endurance characterization, a triangular wave of 3 MV/cm was employed as the scanning/reading electric field, with a scanning frequency of 100 kHz and a reading frequency of 1 kHz. Electrical characterization results revealed that PMA-treated samples exhibited significant wake-up effects, as evidenced by significant polarization enhancement during electrical cycling cycles. Comparative studies demonstrated that samples with Al_2O_{3-x} (H_2O: 10 ms) CL showed significant fluctuations fluctuations in $2P_r$ values compared to the samples with the Al_2O_{3-x} (H_2O: 50 ms) CL. This phenomenon was observed in both PMA and PDA treated samples. Notably, a minimized wake-up effect was observed in the PDA-treated sample with the Al_2O_{3-x} (H_2O: 50 ms) CL. This effect primarily stems from the PDA treatment's effective inhibition of interfacial reaction layer formation between the electrode and (Hf+Zr)O_{2-x} thin films, consistent with literature reports [10, 11]. Furthermore, the CL additionally suppresses the formation of interfacial layers in (Hf+Zr)O_{2-x}, mitigating the redistribution of defect dipoles during polarization cycling, thereby effectively inhibiting the occurrence of wake-up effects [12].

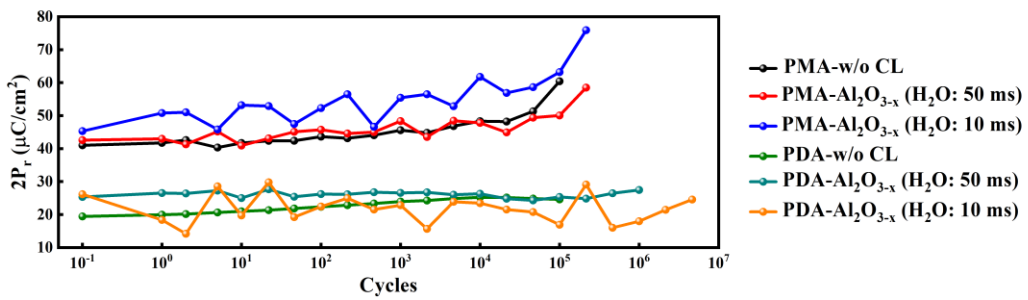

Figure B4 Endurance characteristics of W/CL/(Hf+Zr)O_{2-x}/TiN capacitors after annealing at 550 °C.

Appendix C Material Analysis

Figure C1 displays the GIXRD spectra of the W/CL/(Hf+Zr)O_{2-x}/TiN stack after the

post-metallization annealing (PMA)/post-deposition annealing (PDA) treatment, reveal differences in phase constitutions in all samples. The GIXRD pattern of all samples (excluding the as-deposited sample) exhibits peaks at 28.2°, 30.4°, and 31.4° (2θ), corresponding to the $(\bar{1}11)$ monoclinic phase (28.2°), a superposition of the (111) orthorhombic (o) and (101) tetragonal (t) phases (o+t), and the (111) monoclinic phase (31.4°), respectively [13]. In order to quantitatively characterize the phase content in each sample, all diffraction peaks were deconvoluted with three Gaussian peaks [14]. All fitted peaks are constrained with fixed Full Width at Half Maximum (FWHM) values to ensure the accuracy of the fitting process (as described in the Supplementary Materials). A constant stress must be assumed, which is valid since the stress is largely induced by film densification during crystallization and is less affected by the top electrode [15]. Integrated intensities for each peak were calculated and compared to estimate the relative quantities. As shown in the insert figure, the GIXRD pattern of PMA-treated samples demonstrates a dominant o+t phase peak. Quantitative phase analysis reveals o+t phase fractions of 96.6±0.1% (no CL), 97.8±0.1% (3 cycles of Al_2O_{3-x} (H_2O: 50 ms)), and 98.8±0.1% (3 cycles of Al_2O_{3-x} (H_2O: 10 ms)), respectively. The insertion of the CL led to an increase in the concentration of the o+t phase and minimized the m-phase in the $(Hf+Zr)O_{2-x}$ film. For PDA-treated samples, the concentration of m-phase is higher than that of the corresponding PMA-treated sample. The reference sample without CL exhibits a high proportion of m-phase peaks, primarily attributed to the lack of strain during the annealing process [10]. The o+t phase proportion increased significantly compared with the reference sample after the deposition of the CL, which is consistent with the trends observed from polarization measurements.

GIXRD characterization: For PMA-treated samples, W electrode was removed by 30% H_2O_2 solution after annealing at 550 °C, followed by GIXRD characterization. For PDA-treated samples, GIXRD characterization was performed directly after annealing at 550 °C. The GIXRD curve of the unannealed reference sample is also given, and its diffraction peak comes from the TiN bottom electrode. In GIXRD analysis, differences in the number of atomic planes along different scattering vectors can indeed affect peak width. Additionally, under biaxial stress conditions, strain is closely related to the tilting angle of atomic planes, which may lead to variations in FWHM. In this work, the use of fixed FWHM values for peak fitting was primarily aimed at avoiding uncertainties introduced by multi-parameter fitting, thereby improving the reliability of phase content comparisons across different samples.

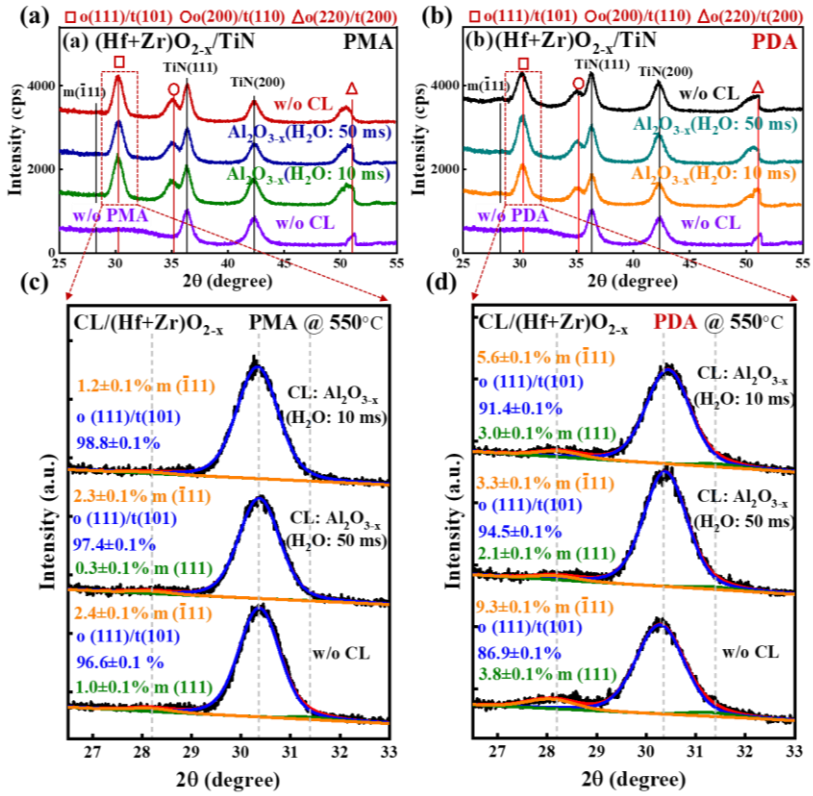

Figure C1 GIXRD patterns of (a) W/CL/(Hf+Zr)O_{2-x}/TiN stack after PMA treatment and (b) CL/(Hf+Zr)O_{2-x}/TiN stack after PDA treatment (CL: w/o CL, Al_2O_{3-x} (H_2O: 50 ms), and Al_2O_{3-x} (H_2O: 10 ms)). Insert: Phase deconvolution of the GIXRD spectra for samples after (c) PMA and (d) PDA treatment, showing the contributions of the ($\bar{1}11$) m (orange line), o+t (blue line), and (111) m (green line) phase. The calculated phase fraction is indicted to the left of each corresponding pattern.

Figure C2(a) shows the deconvoluted Hf 4*f*, Zr 3*d*, O 1*s* and C 1*s* core level spectra for (Hf+Zr)O_{2-x} film after annealing at 550 °C with the take-off angle of 90° and 45°, respectively. The sensitivity factors used for quantification were 59.807 for Hf 4*f*, 57.561 for Zr 3*d*, 14.273 for O 1*s*, and 5.836 for C 1*s* peak. All fitted peaks are constrained with fixed FWHM values to ensure the accuracy of the fitting process in each spectrum. The fitting parameters are used to calculate the atomic ratio of the (Hf+Zr)O_{2-x} ferroelectric films. To compensate the band bending effect and partial charging effect, the C 1*s* spectra of C-C/C-H were referenced to 285 eV. The broad peaks of Hf 4*f* and Zr 3*d* core level spectra in peak fitting make it unreliable to differentiate the oxygen-deficient state from the saturated state. Multi-component fitting attempts introduced substantial uncertainties. Therefore, single-peak fitting was adopted exclusively for elemental ratio quantification. The Hf $4f_{7/2}$ peak and Zr $3d_{5/2}$ are located at 17.50 eV and 182.90 eV, with the doublet splitting of 1.66 eV and 2.40 eV, respectively [16, 17]. The main peak with the binding energy (BE) of 530.82 eV is assigned to the HfO_2/ZrO_2 state in O 1*s* spectra. Three peaks were identified with BE offsets of +0.8 eV (HfO_{2-x}/ZrO_{2-y} oxygen vacancies), +1.8 eV (hydroxyl groups), and +2.8 eV (carbon-oxygen species) [16]. Quantitative analysis showed the oxygen-deficient fraction decreased from 18.8% at 45° to 12.7% at 90°, clearly demonstrating more pronounced oxygen deficiency at the (Hf+Zr)O_{2-x} surface. Consistently, angle-resolved XPS measurements revealed compositional variations

across probing depths, with $Hf_{0.45}Zr_{0.55}O_{1.28}$ at surface-sensitive 45° transitioning to $Hf_{0.44}Zr_{0.56}O_{1.48}$ at bulk-sensitive 90°, further confirming the stoichiometric depth dependence (Table S1). The observed oxygen deficiency in the films agrees well with established findings for HfO_2-based thin films with substantial o-phase content, as documented in prior studies [13, 18].

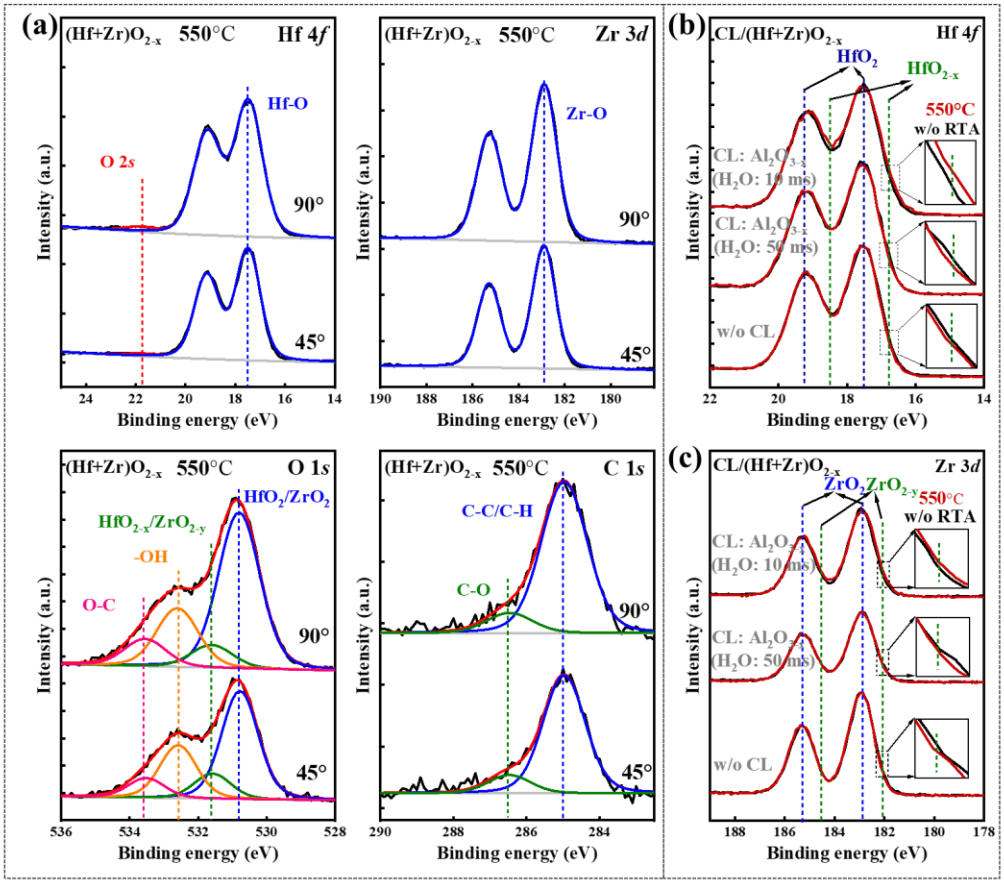

Figure C2 (a) The XPS spectra for Hf 4*f*, Zr 3*d*, O 1*s* and C 1*s* taken with the scan angle of 90° and 45° for $(Hf+Zr)O_{2-x}$ film after annealing at 550 °C. Overlapped (b) Hf 4*f* and (c) Zr 3*d* core level spectra for CL/$(Hf+Zr)O_{2-x}$ stack before and after annealing at 550 °C. Insert: Enlarged portions of the Hf 4*f* and Zr 3*d* core level spectra at lower oxidation state.

Table S1 The fitted areas and sensitivity factors of Hf/Zr-O peak in the O 1*s*, Hf 4*f*, and Zr 3*d* spectra of the reference samples.

Core level	State	Area		ASF
		45°	90°	
Hf 4*f*	Hf-O	10421	13261	59.807
Zr 3*d*	Zr-O	12225	16135	57.561
O 1*s*	O-Hf/Zr	7021	10567	14.273

The XPS data were characterized without the top electrode to directly investigate the modulation effect of Al_2O_{3-x} CL on the oxygen chemical states at the upper interface of $(Hf+Zr)O_{2-x}$ films. As shown in figure C2(b)-(c), the normalized Hf 4*f* and Zr 3*d* core level spectra for the samples with no CL (w/o CL), Al_2O_{3-x} (H_2O: 50 ms) CL, and Al_2O_{3-x} (H_2O: 10 ms) CL were compared before and after annealing. The results clearly demonstrate

that the introduction of an Al_2O_{3-x} (H_2O: 10 ms) CL leads to a significant increase in HfO_{2-x}/ZrO_{2-y} content after annealing. In contrast, for the samples without CL and Al_2O_{3-x} (H_2O: 50 ms) CL samples, the oxygen-deficient states (HfO_{2-x}/ZrO_{2-y}) exhibit a slight reduction after annealing, which may be attributed to the partial oxidation of the $(Hf+Zr)O_{2-x}$ film by -OH groups during annealing treatment, consistent with previous reports [16]. Furthermore, in the case of insertion Al_2O_{3-x} (H_2O: 50 ms) CL sample, the decrease in oxygen-deficient states could also be influenced by oxygen migration from the Al_2O_{3-x} (H_2O: 50 ms) layer. However, due to the limited thickness of the CL, the Al 2*p* signal exhibited poor signal-to-noise ratio, preventing reliable observation of Al-related chemical changes in the spectra. As evidenced by the normalized Hf 4*f* and Zr 3*d* spectra in Figure C3, the Al_2O_{3-x} (H_2O: 10 ms)-capped sample developed substantially more intense sub-oxide features (HfO_{2-x}/ZrO_{2-y}) than the Al_2O_{3-x} (H_2O: 50 ms) CL sample after annealing at 550 °C. These results suggest that insertion of Al_2O_{3-x} thin films effectively modulate the oxygen vacancy concentration near the $(Hf+Zr)O_{2-x}$ surface. Meanwhile, the variation in interfacial oxygen vacancy concentration observed in XPS spectra shows good agreement with the *P-V* measurement results, indicating that samples with higher interfacial oxygen vacancy concentrations exhibit more pronounced changes in P_r values at low frequencies. This phenomenon is likely attributed to the combined effects of charge trapping/detrapping effects at the interface and the migration of oxygen ion/vacancy.

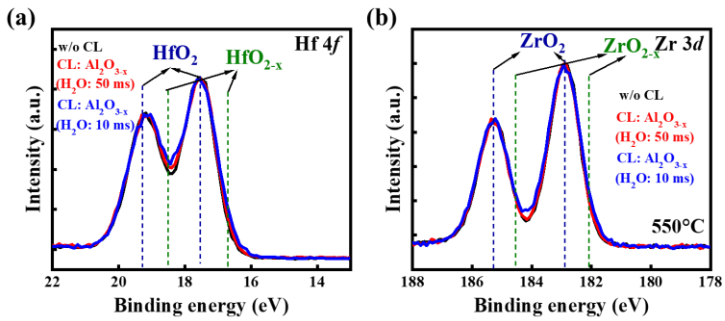

Figure C3 Overlapped (a) Hf 4*f* and (b) Zr 3*d* core level spectra for CL/$(Hf+Zr)O_{2-x}$ stack after annealing at 550 °C.

XPS analysis revealed that the BE of the Al 2*p* peak remained nearly identical for the samples with Al_2O_{3-x} CL (possessing different oxygen deficiency levels). A significant shift in the Hf 4*f* peak was observed (all data were calibrated using the C 1*s* peak at 285 eV). This peak shift is associated with interfacial dipole. The formation of interfacial dipole primarily stems from the difference in planar charge density of oxygen atoms between Al_2O_{3-x} and $(Hf+Zr)O_{2-x}$ (with oxygen atoms slightly shifting from $(Hf+Zr)O_{2-x}$ toward Al_2O_{3-x}). The higher oxygen deficiency in the Al_2O_{3-x} (H_2O: 10 ms) layer indicates stronger interfacial dipole intensity in this sample. The presence of interfacial dipoles reduces the kinetic energy of photoelectrons emitted from the $(Hf+Zr)O_{2-x}$ side (manifested as an increase in the BE of Hf 4*f* peak), which aligns with our XPS observations.

Figure C4(a)-(l) illustrates the elemental distribution in capacitors after applied positive/negative pulse (after multiple polarization switching cycles, ±3 V pulses with 100

μs duration were applied), with intensities normalized using Cs^{2+} and Cs^{+} as references. The interfaces between the top/bottom electrodes and the CL/$(Hf+Zr)O_{2-x}$ stack were determined by the midpoint of the highest intensity positions of W and TiN, as marked by dashed lines. After a positive pulse, $^{18}O^{+}$ accumulates predominantly at the CL/$(Hf+Zr)O_{2-x}$ interface. Conversely, after a negative pulse, the $^{18}O^{+}$ concentration increases significantly at the $(Hf+Zr)O_{2-x}$/TiN interface compared to the top interface. Both additional post-bias characterization datasets show consistent results (Figure S8). This observation is further supported by the distribution of $CsAl^{18}O^{+}$ cluster ions, which exhibit accumulation at both interfaces under negative bias. These results demonstrate long-range migration of oxygen ions ($^{18}O^{2-}$) from the CL under an applied electric field. The migration behavior of oxygen ions at the interface exhibits coupling with ferroelectric polarization switching in HfO_2-based devices, consistent with theoretical models reported in the literature [3, 19]. The origin of mobile oxygen ions can be rationalized through several potential mechanisms based on previous studies. Ideally, direct contact between W/TiN and the oxide would lead to an oxygen scavenging effect, which may result in the formation of movable oxygen ion/vacancy pairs at the interface [14, 20, 21]. Considering the bond dissociation energies of W–O (675 kJ/mol), Hf–O (801±13 kJ/mol), Zr–O (766.1±10.6 kJ/mol), Al-O (402 kJ/mol), and Al^{+}-O (~160 kJ/mol) in the stack, bond dissociation is more likely to occur in the CL[22]. This suggests that the capacitor with a CL, particularly when using an Al_2O_{3-x} layer, may exhibit a higher concentration of interfacial oxygen ions/vacancies at the W/CL/$(Hf+Zr)O_{2-x}$ interface, which leads to a larger P_r difference between 500 Hz and 1 kHz. Oxide films deposited by ALD should be electrically neutral, and oxygen vacancies in $(Hf+Zr)O_{2-x}$ may provide pathways for the migration of O^{2-}/ V_O^{2+} at the interface [17]. The migration barrier for O^{2-}/ V_O^{2+} is hypothesized to be lower in the oxygen-deficiency $(Hf+Zr)O_{2-x}$ film [23]. Therefore, the moveable O^{2-} at the interface can undergo long-range migration in the $(Hf+Zr)O_{2-x}$ film under an applied bias.

Figure C4(m) illustrates a polarization switching model combining ferroelectric dipoles, charge trapping/detrapping, and interfacial oxygen ion/vacancy migration under low-frequency excitation. The movement of interfacial oxygen ion-vacancy pairs across the $(Hf+Zr)O_{2-x}$ layer is primarily driven by the electric field, aligning the long-range dipoles formed by these movable ion-vacancy pairs with the polarization direction of the ferroelectric crystal dipoles. Additionally, charge trapping/detrapping at defect sites modulates the local electric field, further influencing the alignment dynamics of these dipoles. Thus, the $2P_r$ value is highest at low frequency. Notably, the ferroelectric polarization is suppressed by long-range ion/vacancy migration and charge trapping/detrapping effects during low-frequency cycling, which is consistent with literature [3]. As the testing frequency increases, the migration process of O^{2-}/V_O^{2+} and charge trapping/detrapping process declines significantly, ultimately limiting their collective response to the field. During this process, the differing frequency response capabilities of long-range dipoles, charge traps, and ferroelectric crystal dipoles cause

competition among those polarization mechanisms, which may explain the fluctuating $2P_r$ values observed in the sample with Al_2O_{3-x} (H_2O: 10 ms) CL during endurance characterization. By decoupling the roles of ferroelectric dipoles, charge traps, and ionic migration, this model advances the understanding of polarization dynamics in HfO_2-based ferroelectric systems.

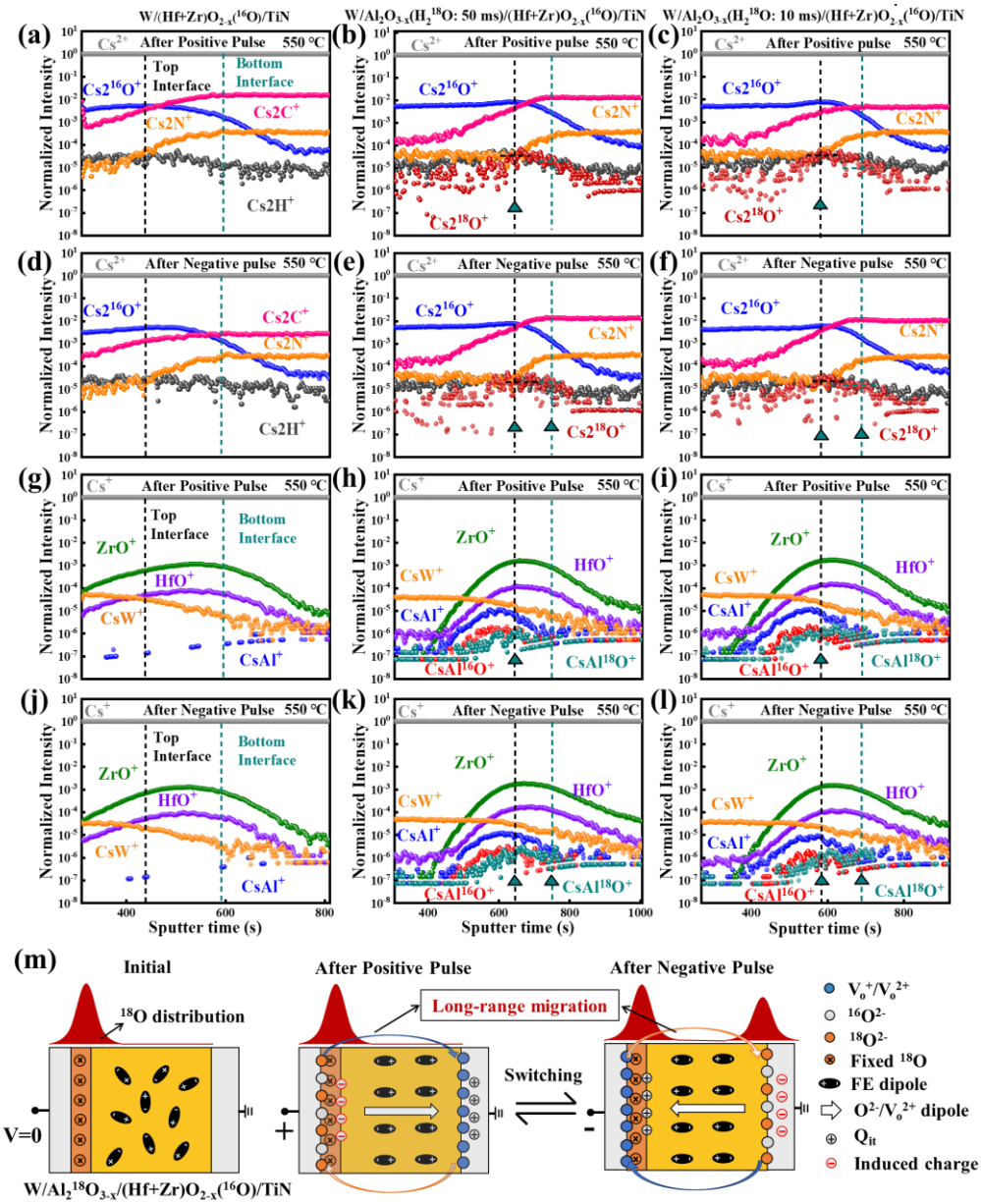

Figure C4 TOF-SIMS depth profiles of (a)–(f) oxygen isotopes ($Cs2^{16}O^+$, $Cs2^{18}O^+$), nitrogen ($Cs2N^+$), carbon ($Cs2C^+$) and hydrogen ($Cs2H^+$), and (g)–(l) metallic species (CsW^+, $CsHf^+$, $CsZr^+$, $CsAl^+$, $CsAl^{16}O^+$, and $CsAl^{18}O^+$) in W/CL/$(Hf+Zr)O_{2-x}$/TiN capacitors after positive/negative pulse. (m) Schematic diagram of the $(Hf+Zr)O_{2-x}$ polarization and interfacial ion migration model.

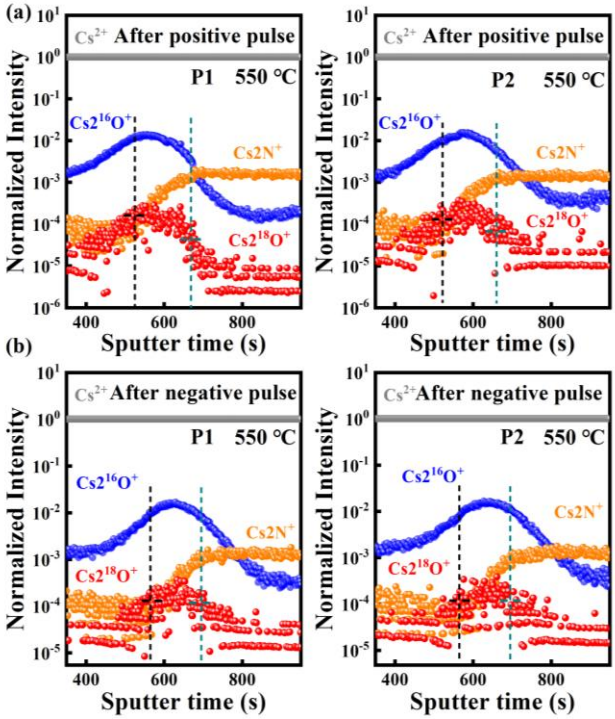

Figure C5 TOF-SIMS depth profiles of oxygen isotopes ($Cs2^{16}O^+$, $Cs2^{18}O^+$), nitrogen ($Cs2N^+$) in W/CL/$(Hf+Zr)O_{2-x}$/TiN capacitors after (a) positive and (b) negative pulse application (2 measurement points per bias condition).

Experimentally, the delay between applied electrical pulse and characterization was strictly controlled within 24 hours. All SIMS characterizations were performed without an external voltage applied while maintaining grounding of the bottom electrode during measurements. TOF-SIMS profiling required approximately 0.5 hours per device.

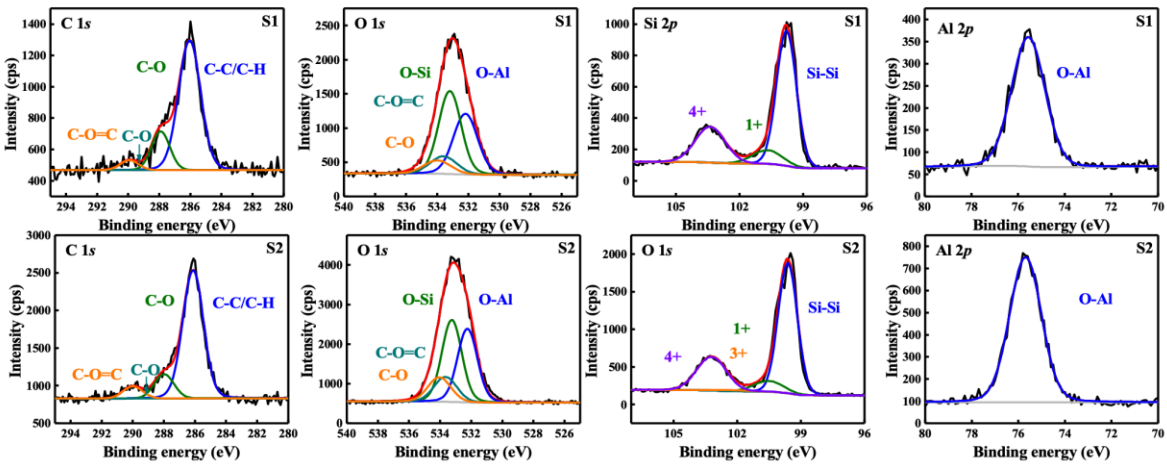

Figure C6 The C 1*s*, O 1*s*, Si 2*p* and Al 2*p* core level spectra for (a) Al_2O_{3-x} (H_2O: 50 ms)/Si stack and Al_2O_{3-x} (H_2O: 10 ms)/Si stack.

The ALD process of Al_2O_{3-x} may introduce impurities such as C and H. However, the use of only 3 ALD cycles for the Al_2O_{3-x} CL effectively limits the total impurity content. Although residual -CH_3 groups (from TMA precursor) may exist due to incomplete precursor reactions during ALD deposition, thermal annealing can reduce these organic ligands according to literature [24]. In this work, no C-related energy loss peak was detected in the C 1*s* XPS spectrum. The observed C signal may mainly come from

ambient adsorption during *ex-situ* deposition. Meanwhile, no significant C impurity peak was observed in the Al_2O_{3-x} film in TOF-SIMS spectra (Figure C4-C5). The weak H peak at the W/Al_2O_{3-x}/$(Hf+Zr)O_{2-x}$ interface (Figure C4-C5) indicate that the H signal mainly comes from the $(Hf+Zr)O_{2-x}$ layer. The presence of -OH groups in $(Hf+Zr)O_{2-x}$ ferroelectric has been widely reported [10, 16, 25] and was also observed in our XPS data.

The stoichiometric ratios were derived from XPS quantitative analysis based on the intensity ratio between the Al-O bond peak in the Al 2*p* spectrum and the O-Al bond peak in the O 1*s* spectrum, calculated using the formula: $\frac{\text{Area}_{\text{Al-O}}}{ASF_{Al\ 2p}}:\frac{\text{Area}_{\text{O-Al}}}{ASF_{O\ 1s}}$, where ASF denotes atomic sensitivity factors. For the Al_2O_{3-x} film deposited with 50 ms H_2O pulses, the composition corresponds to $Al_2O_{2.9}$. With the H_2O pulse duration shortened to 10 ms, the resulting Al_2O_{3-x} film demonstrates a composition of AlO.

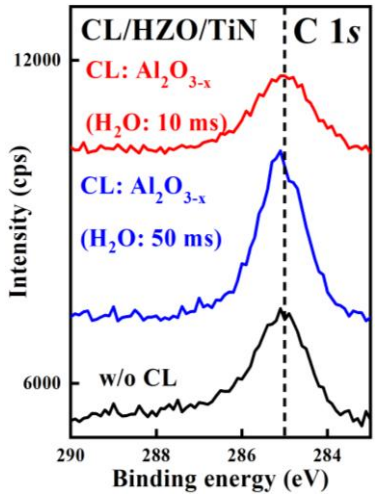

Figure C7 The C 1*s* core level spectra for CL/$(Hf+Zr)O_{2-x}$/TiN stack after annealing at 550 °C.

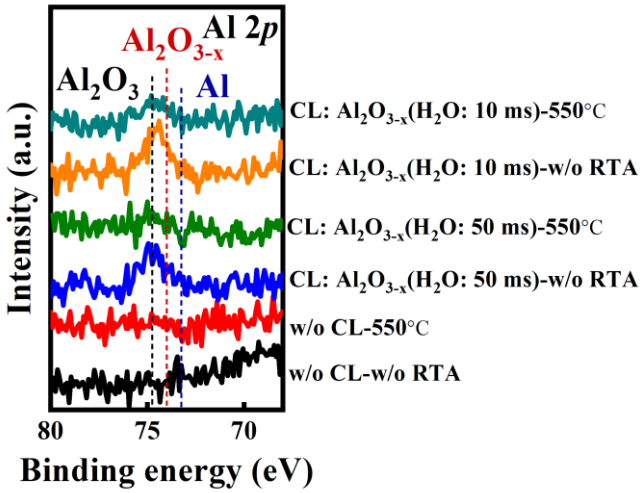

Figure C8 Al 2*p* core level spectra of 8 nm-$(Hf+Zr)O_{2-x}$/TiN stack, Al_2O_{3-x} (H_2O: 50 ms)/$(Hf+Zr)O_{2-x}$/TiN stack, and Al_2O_{3-x} (H_2O: 10 ms)/$(Hf+Zr)O_{2-x}$/TiN stack before and after annealing at 550 °C.

The chemical formulas of HZO were derived from XPS peak-fitting quantification, where $Hf_{0.45}Zr_{0.55}O_{1.28}$ represents surface-sensitive 45° take-off angle data, and

$Hf_{0.44}Zr_{0.56}O_{1.48}$ corresponds to bulk-sensitive 90° data. The calculation followed standard XPS quantitative methods (peak area/atomic sensitivity factors), with parameters listed in Table S1.

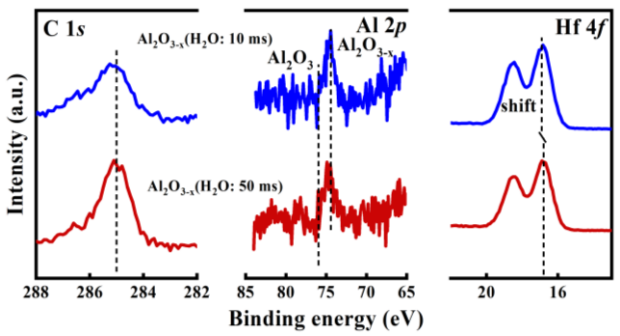

Figure C9 The C 1*s*, Al 2*p* and Hf 4*f* core level spectra for Al_2O_{3-x}/(Hf+Zr)O_{2-x} stacks.

References

[1] Kaya S, Yilmaz E, Aktag A, Seidel J 2015 Characterization of interface defects in $BiFeO_3$ metal–oxide–semiconductor capacitors deposited by radio frequency magnetron sputtering. *J. Mater. Sci. Mater. Electron.* 26 5987-5993.

[2] Xiao H, Huang S 2010 Frequency and voltage dependency of interface states and series resistance in Al/SiO_2/p-Si MOS structure. *Mater. Sci. Semicond. Process.* 13 395-399.

[3] Li K, Peng Y, Xiao W, Liu F, Zhang Y, Feng Z, Dong H, Liu Y, Hao Y, Han G 2023 A comparative study on the polarization, reliability, and switching dynamics of HfO_2-ZrO_2-HfO_2 and ZrO_2-HfO_2-ZrO_2 superlattice ferroelectric films. *IEEE Trans. Electron Devices*. 70 1802-1807.

[4] Peng Y, Wang Z, Xiao W, Ma Y, Liu F, Deng X, Yu X, Liu Y, Han G, Hao Y 2022 Effect of thickness scaling on the switching dynamics of ferroelectric HfO_2–ZrO_2 capacitors. *Ceram. Int.* 48 28489-28495.

[5] Yoo HK, Kim JS, Zhu Z, Choi YS, Yoon A, MacDonald MR, Lei X, Lee TY, Lee D, Chae SC, et al., editors. Engineering of ferroelectric switching speed in Si doped HfO_2 for high-speed 1T-FERAM application. 2017 IEEE International Electron Devices Meeting (IEDM); 2017 2-6 Dec. 2017.

[6] Yang SM, Jo JY, Kim TH, Yoon JG, Song TK, Lee HN, Marton Z, Park S, Jo Y, Noh TW 2010 AC dynamics of ferroelectric domains from an investigation of the frequency dependence of hysteresis loops. *Phys. Rev. B*. 82 174125.

[7] Silibin MV, Belovickis J, Svirskas S, Ivanov M, Banys J, Solnyshkin AV, Gavrilov SA, Varenyk OV, Pusenkova AS, Morozovsky N, et al. 2015 Polarization reversal in organic-inorganic ferroelectric composites: Modeling and experiment. *Appl. Phys. Lett.* 107 142907.

[8] Deng S, Zhao Z, Kim YS, Duenkel S, MacMahon D, Tiwari R, Choudhury N, Beyer S, Gong X, Kurinec S, et al. 2022 Unraveling the dynamics of charge trapping and de-trapping in ferroelectric FETs. *IEEE Trans. Electron Devices*. 69 1503-1511.

[9] Muller J, Boscke TS, Schroder U, Mueller S, Brauhaus D, Bottger U, Frey L, Mikolajick T 2012 Ferroelectricity in simple binary ZrO_2 and HfO_2. *Nano Lett.* 12 4318-4323.

[10] Zhou J, Guan Y, Meng M, Hong P, Ning S, Luo F 2024 Improving the endurance for ferroelectric $Hf_{0.5}Zr_{0.5}O_2$ thin films by interface and defect engineering. *Appl. Phys. Lett.* 124 092904.

[11] Peng HK, Chiu CY, Kao YC, Wu PJ, Wu YH 2022 Enhanced reliability, switching speed and uniformity for ferroelectric $HfZrO_x$ on epitaxial Ge film by post deposition annealing for oxygen vacancy control. *IEEE Trans. Electron Devices*. 69 4002-4009.

[12] Chen H, Luo H, Yuan X, Zhang D 2022 Realization of excellent ferroelectricity in PDA-derived $Hf_{0.5}Zr_{0.5}O_2$ films through insertion of an ultrathin Ti metal layer. *Scripta Mater.* 217 114758.

[13] Fields SS, Cai T, Jaszewski ST, Salanova A, Mimura T, Heinrich HH, Henry MD, Kelley KP, Sheldon BW, Ihlefeld JF 2022 Origin of ferroelectric phase stabilization via

the clamping effect in ferroelectric hafnium zirconium oxide thin films. *Adv. Electron. Mater.* 8 2200601.

[14] Alcala R, Materano M, Lomenzo PD, Vishnumurthy P, Hamouda W, Dubourdieu C, Kersch A, Barrett N, Mikolajick T, Schroeder U 2023 The electrode-ferroelectric interface as the primary constraint on endurance and retention in HZO-based ferroelectric capacitors. *Adv. Funct. Mater.* 33 2303261.

[15] Materano M, Mittmann T, Lomenzo PD, Zhou C, Jones JL, Falkowski M, Kersch A, Mikolajick T, Schroeder U 2020 Influence of oxygen content on the structure and reliability of ferroelectric $Hf_xZr_{1-x}O_2$ layers. *ACS Appl. Electron. Mater.* 2 3618-3626.

[16] Feng Z, Peng Y, Liu H, Sun Y, Wang Y, Meng M, Liu H, Wang J, Wu R, Wang X, et al. 2019 The band structure change of $Hf_{0.5}Zr_{0.5}O_2$/Ge system upon post deposition annealing. *Appl. Surf. Sci.* 488 778-782.

[17] Feng Z, Peng Y, Shen Y, Li Z, Wang H, Chen X, Wang Y, Jing M, Lu F, Wang W, et al. 2021 Ferroelectric-like behavior in TaN/high-k/Si system based on amorphous oxide. *Adv. Electron. Mater.* 7 2100414.

[18] Pal A, Narasimhan VK, Weeks S, Littau K, Pramanik D, Chiang T 2017 Enhancing ferroelectricity in dopant-free hafnium oxide. *Appl. Phys. Lett.* 110 022903.

[19] Ma L, Wu J, Zhu T, Huang Y, Lu Q, Liu S 2023 Ultrahigh oxygen ion mobility in ferroelectric hafnia. *Phys. Rev. Lett.* 131 256801.

[20] Huan Liu FY, Bing Chen, Zheng-Dong Luo, Jiajia Chen, Yong Zhang, Ze Feng, Hong Dong, Xiao Yu, Yan Liu, Genquan Han and Yue Hao 2024 Evidence for reversible oxygen ion movement during electrical pulsing: enabler of emerging ferroelectricity in binary oxides. *Materials Futures*. 3 11pp.

[21] Segantini G, Manchon B, Cañero Infante I, Bugnet M, Barhoumi R, Nirantar S, Mayes E, Rojo Romeo P, Blanchard N, Deleruyelle D, et al. 2023 Interplay between strain and defects at the interfaces of ultra-thin $Hf_{0.5}Zr_{0.5}O_2$-based ferroelectric capacitors. *Adv. Electron. Mater.* 9 2300171.

[22] Luo YR. *Comprehensive Handbook of Chemical Bond Energies (CRC Press)*2007.

[23] Hu Y, Wang C, Dong H, Wallace RM, Cho K, Wang W-H, Wang W 2016 Origin of indium diffusion in high-k oxide HfO_2. *ACS Appl. Mater. Interfaces*. 8 7595-7600.

[24] LU Hong-Liang XM, DING Shi-Jin,REN Jie,ZHANG Wei. 2006 Thermal stability of atomic layer deposition Al_2O_3 thin films. *Journal of Inorganic Materials*. 21 1217-1222.

[25] Hill MO, Kim JS, Müller ML, Phuyal D, Taper S, Bansal M, Becker MT, Bakhit B, Maity T, Monserrat B, et al. 2024 Depth-resolved X-ray photoelectron spectroscopy evidence of intrinsic polar states in HfO_2-based ferroelectrics. *Adv. Mater.* 36 2408572.